

Architecture in Stiff Biological Materials: a Template for Toughness Enhancement, or a Siren Song?

Michael A. Monn¹, Kaushik Vijaykumar¹, Sayaka Kochiyama¹, and Haneesh Kesari*¹

¹*School of Engineering, Brown University, Providence, RI, USA*

Keywords: structure-property relationships, *Euplectella aspergillum*, fracture toughness, R-curves, biological composites

Some stiff biological materials, such as shells and bones, have surprisingly high fracture toughness compared to their brittle ceramic constituents. These materials are heterogeneous and consist of layers of ceramic phases separated by thin organic interlayers. Understanding the link between layered architectures and toughness could help to identify new ways to improve the toughness of engineering composites. We study one instance of the layered architecture found in the skeletal elements—called spicules—of the marine sponge *Euplectella aspergillum*. The spicules contain cylindrical layers composed of silica. We cut micrometer-size notches in the spicules and perform flexural tests on them to measure their fracture initiation toughness and average crack growth resistance. We found that the spicule’s architecture provides up to a ten-fold enhancement to its fracture initiation toughness. We also found that it provides approximately a two-fold enhancement to its average crack growth resistance. However, compared to some other prototypically tough biological materials, like nacre, the toughness enhancements provided by the spicule’s architecture are relatively small. We investigate the reasons underlying the lack of toughness enhancement using computational fracture mechanics simulations. The combination of mechanical characterization and computational mechanics simulations presented here provides a framework for developing a more complete understanding of how toughness enhancing mechanisms can be induced or suppressed by changing the geometry of a layered architecture.

- 1 Despite being primarily composed of brittle ceramics, some stiff biological materials (SBMs), such as
- 2 bones and shells, are remarkably tough^[1–4]. For example, nacre—the iridescent material found in mol-
- 3 lusk shells—is composed of >95% aragonite (a brittle, calcium carbonate mineral) by volume yet it has
- 4 a specific fracture initiation toughness on par with nylon and some iron alloys^[4]. A material’s fracture
- 5 initiation toughness quantifies its ability to prevent the growth of pre-existing cracks or flaws, and there-
- 6 fore be resistant to catastrophic failure. These tough SBMs are often heterogeneous and are composed
- 7 of alternating layers of ceramic and organic materials (see **Figure 1**). The arrangements of these layers,
- 8 which we refer to as layered architectures, are thought to be responsible for the toughness enhancements

9 observed in these SBMs^[5]. There is currently considerable interest in understanding the connections be-
10 tween layered architectures and toughness enhancements in SBMs^[5–8] because this understanding could aid in the development of new, tough engineering materials^[4, 9, 10].

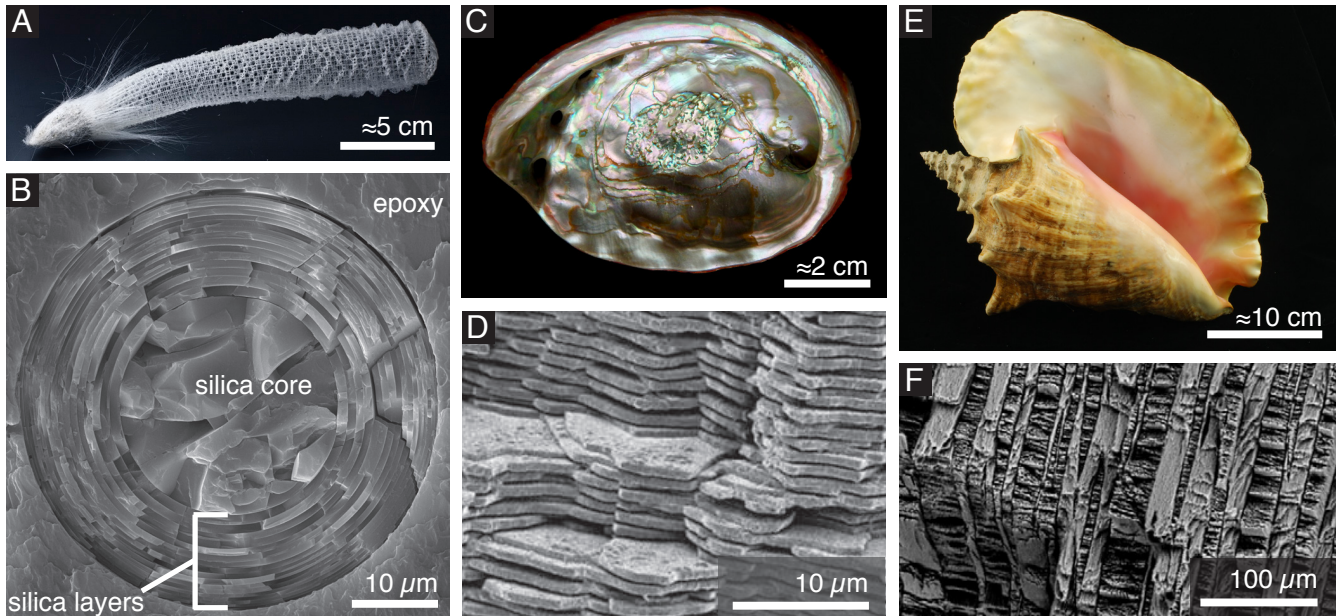


Figure 1. Examples of the layered architecture in SBMs. (A) Skeleton of a *Euplectella aspergillum* sponge (modified from^[11] copyright 2015, The National Academy of Sciences). (B) Concentric silica layers make up the cylindrical layered architecture of anchor spicules from *E. aspergillum* (modified from^[11] copyright 2015, The National Academy of Sciences). (C) The iridescent shell of *Haliotis rufescens* (courtesy of John Varner). (D) The brick and mortar layered architecture of nacre consisting of staggered aragonite tablets (modified with permission from^[12] copyright 2012, the Royal Society of Chemistry). (E) The shell of the queen conch (*Strombus gigas*) (courtesy of John Varner). (F) The crossed-layered architecture of the *S. gigas* shell, which consists of layers of aragonite (modified with permission from^[13] copyright 2014, Elsevier).

11
12 A number of SBMs, including nacre and bone, have served as models for the seminal research on un-
13 derstanding these connections^[14, 15]. Recently, the anchor spicules of the marine sponge *Euplectella*
14 *aspergillum* (*Ea.*) have been added to this group of model SBMs^[5, 6, 8, 16]. The anchor spicules are hair-
15 like fibers that attach *Ea.* to the soft sediment of the sea floor where it lives (see **Figure 2** (A)–(B))^[17].
16 Each of the thousands of anchor spicules in a *Ea.* sponge is approximately 10 cm long and 50 μm in
17 diameter. Viewed in cross-section, an anchor spicule consists of a solid cylindrical core surrounded by
18 ≈ 25 concentric, cylindrical layers (see Figure 1(B) and 2(C))^[11, 17, 18]. Both the core and the layers
19 are composed of silica and adjacent silica layers are separated by a thin ($\approx 5\text{--}10 \text{ nm}$)^[17] organic inter-
20 layer. Similar cylindrical layered architectures have also been found in spicules from a number of related
21 sponge species^[19–22].
22 Many previous studies of *Ea.* anchor spicules suggest that like the layered architectures of nacre and other

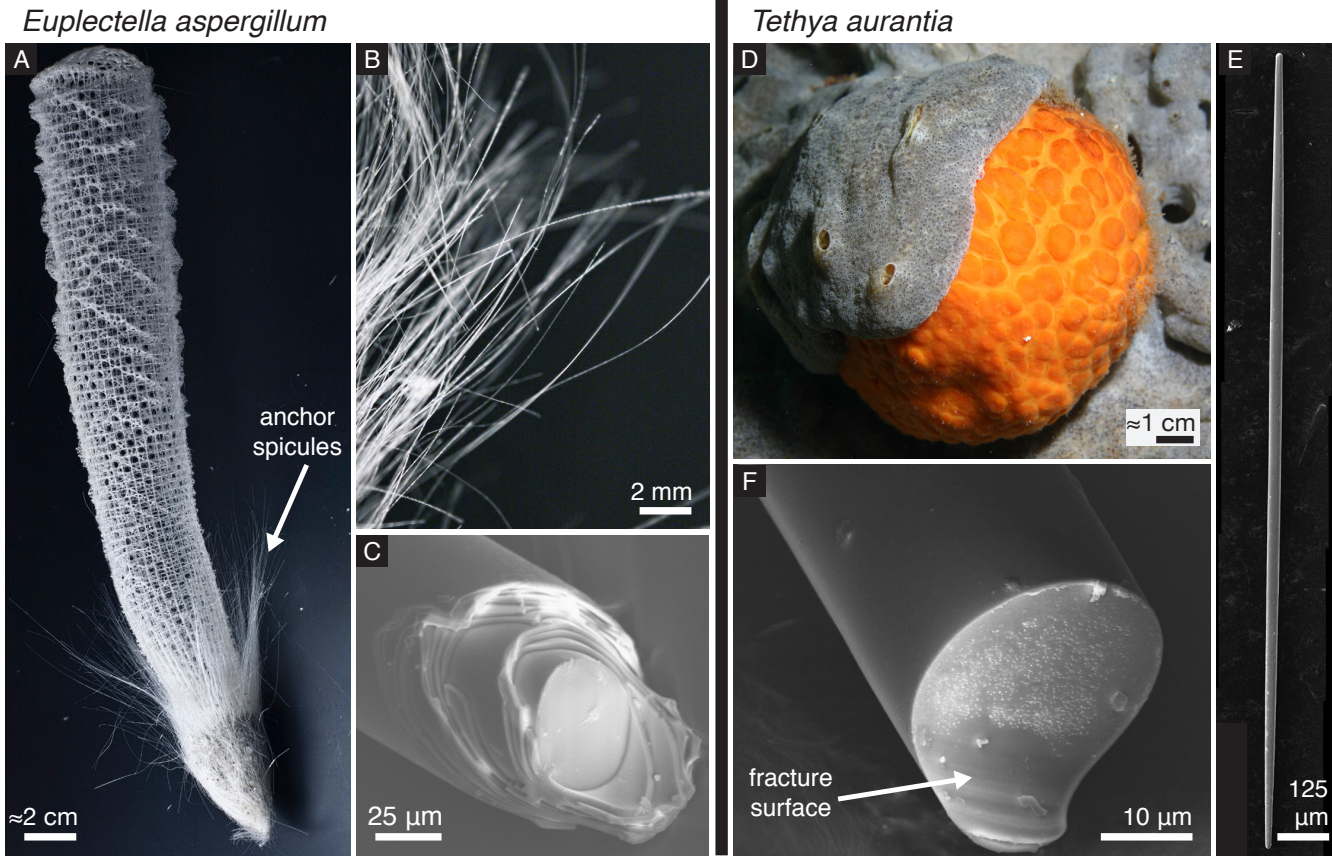


Figure 2. The skeletons and spicules of *Ea.* and *Ta.* sponges. (A) The skeleton of the *Ea.* sponge (modified from^[11] copyright, the National Academy of Sciences). (B) The anchor spicules that fasten the sponge to the seafloor (modified from^[11] copyright, the National Academy of Sciences). (C) The broken end of an *Ea.* anchor spicule that was fracture in three-point bending showing its layered architecture (modified from^[23] copyright 2017, Elsevier). (D) A *Ta.* sponge (image courtesy of Steve Lonhart/NOAA MBNMS). (E) A toothpick-like spicule found within the *Ta.* sponge (reproduced from^[24] under the Creative Commons 4.0 BY license). (F) The exposed surface of a *Ta.* spicule that was fractured in the same way as the *Ea.* spicule shown in (C) showing that it does not contain a layered architecture (modified from^[23] copyright 2017, Elsevier).

23 tough SBMs, the spicule's cylindrical layered architecture also enhances fracture toughness^[5,6,8,16].
 24 None of these studies, however, provide direct measurements of the *Ea.* spicule's fracture toughness, nor
 25 by other means do they quantify how much the architecture enhances the spicule's toughness compared
 26 to that of its constituent silica. These measurements and comparison are critical for determining whether
 27 the *Ea.* spicules should be used as a template for bioinspired materials with enhanced toughness.
 28 We measured the *Ea.* spicule's fracture toughness by cutting micrometer-size notches in the spicules
 29 using a focused ion beam and performing flexural tests on them (see Section 2.1). The notches ranged
 30 in length from approximately 7% to 64% of the spicule's diameter. During the flexural test, a notched
 31 spicule was bent until a crack grew from the notch and fractured it (see Figure 3(A)–(B)). We measured
 32 the force applied to a spicule during the test and the lateral deflection of its cross-section at the location

33 the load was applied. Using these data, we computed the spicule's fracture toughness (see Sections 2.3
34 and 2.4).

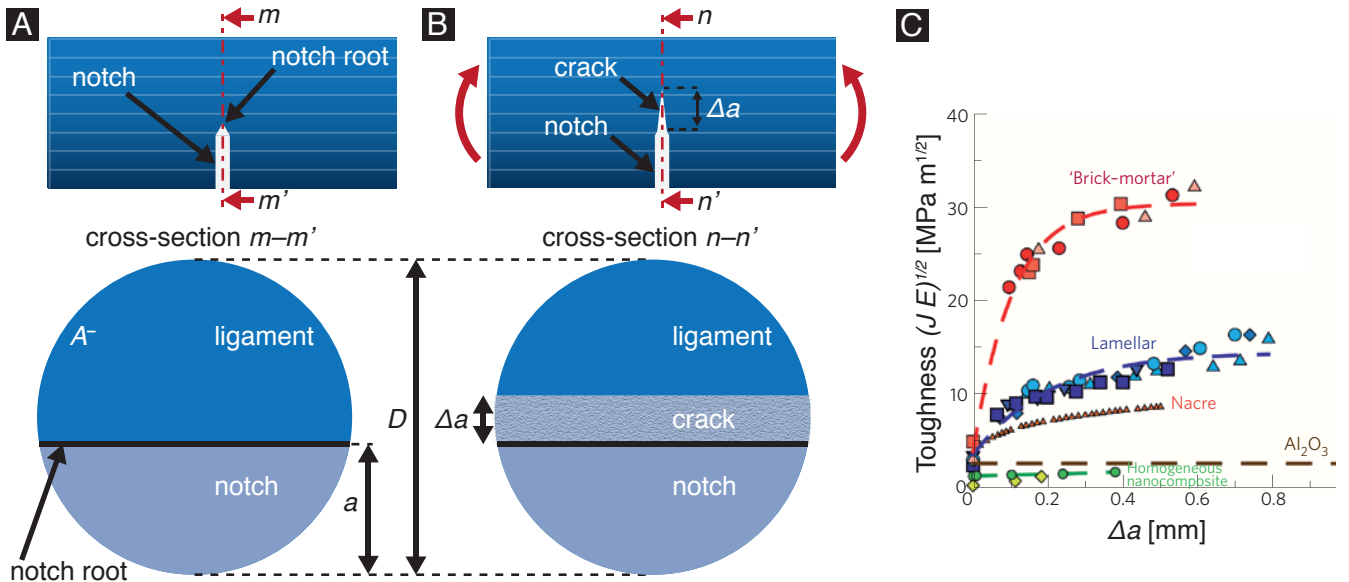
35 To quantify the toughness enhancement provided by the *Ea.* spicule's architecture, we compared its
36 fracture toughness to the fracture toughness of spicules from a related sponge, *Tethya aurantia* (*Ta.*) (see
37 Figure 2(D)–(F)). The *Ta.* spicules have a similar chemical composition and bonding structure to the *Ea.*
38 spicules^[20], but do not possess a layered architecture (see Figure 2(F))^[24]. They are ≈2 mm long, ≈35
39 μm in diameter and have a needle-like shape. That is, they are thickest at the midpoint along their length
40 and taper to become thinner toward their ends (see Figure 2(E)). We measured the *Ta.* spicules' fracture
41 toughness using the same type of notched flexural test that we performed on the *Ea.* spicules (see Section
42 2).

43 Overall, we found that the toughness enhancement provided by the *Ea.* spicule's architecture is much
44 smaller than that provided by architectures seen in prototypically tough SBMs, like nacre and bone (see
45 Section 2.5). While these tough SBMs also possess layered architectures, the layers in these materials are
46 flat rather than cylindrical/curved (see Figure 1). For very short notches (less than 10% of the spicule's
47 diameter), we observed that the *Ea.* spicule's architecture did provide up to a 10 fold increase in fracture
48 initiation toughness. However, this enhancement is still relatively small compared to that observed in
49 nacre. This observed increase in fracture initiation toughness is consistent with the crack tip shielding
50 effect described by^[25]. We discuss the increased initiation toughness enhancement for short notches in
51 greater detail in Section 2.3.

52 We investigated the difference in the toughness enhancements provided by the cylindrical and flat layered
53 architectures using computational mechanics simulations (see Section 3). In the simulations we used
54 a regularized variational fracture method^[26] to predict how both cylindrical and flat layers affect crack
55 growth. We compared the mechanical response and crack pattern in a specimen containing two cylindrical
56 layers to a specimen containing two flat layers. We found that while crack arrest and re-nucleation
57 appears to be the dominant toughening mechanism in the flat layered architecture, it does not manifest
58 to the same extent in the cylindrical layered architecture. Thus, the curvature of the *Ea.* spicules' layers
59 could fundamentally change the toughening mechanisms operating within them compared to SBMs with
60 flat layered architectures.

61 1 Recapitulation of the concept of fracture toughness

62 Roughly speaking, fracture toughness—also known as crack growth resistance, R —is the amount of
 63 energy that a crack consumes to grow its area by a unit amount. If the energy consumed does not depend
 64 on the geometries of the crack, the crack increment, the specimen, and the specimen's architecture then
 65 R is considered to be a material property. However, in SBMs the value of R can depend on the length that
 66 the crack has grown, Δa (see **Figure 3(B)–(C)**). The value of R when a crack first starts growing, $R(0)$, is
 67 known as the fracture initiation toughness. If the value of R increases with Δa , then the material is said to
 68 have a rising R curve (see e.g., Figure 3(C)). In this case, as the crack grows the material becomes more
 69 resistant to crack growth. Several SBMs like nacre and bone^[7,27–29] as well as in synthetic materials with
 70 architectures inspired by these SBMs (see Figure 3(C))^[1] display rising R curves. In these materials, the
 71 rise in R is caused by toughening mechanisms that become activated as a crack grows and interacts with
 the layered architecture.



72
Figure 3. Fracture toughness. (A) Geometry of a fracture test specimen with a notch cut in it. A cross-sectional view shows
 73 the notch length, a , and ligament area, A^- . (B) When loaded in flexure, a crack grows from the notch root. The crack length,
 74 Δa is shown in the corresponding cross-sectional view. (C) Crack growth resistance curves of nacre, nacre-inspired composites
 75 made of aluminum oxide tablets, and monolithic aluminum oxide obtained by^[1] and^[9]. The crack growth resistance is given
 here in terms of the J -integral (modified with permission from^[1] copyright Nature Publishing Group).

72

73 We measured $R(0)$ and $\langle R \rangle$ —i.e., the average value of R (see Section 2.4 for details)—for the *Ea.* anchor
 74 spicules and the *Ta.* spicules (see Section 2). By comparing $R(0)$ and $\langle R \rangle$ of the *Ea.* spicules to $R(0)$
 75 and $\langle R \rangle$ of the *Ta.* spicules, we quantified the toughness enhancement provided by the *Ea.* spicule's

Table 1. Summary of specimen geometry (see Figure 4 for *Ea.* and *Ta.* spicules^{a)}. Values for diameter (D), span (L) and notch length (a) listed as mean±standard error of measurement

Species	No. specimens	L [μm]	D [μm]	a [μm]
<i>E. aspergillum</i>	35	799.25±6.35	41.42±2.16	12.92±1.30
<i>T. aurantia</i>	26	725.86±18.36	32.28±1.07	6.96±0.80

^{a)} see Tables S1 and S2 for details of the geometry of individual *Ea.* and *Ta.* specimens.

76 architecture both at fracture initiation and during crack growth (see Section 2.5).

77 2 Results

78 To measure $R(0)$ and $\langle R \rangle$, we performed flexural tests on 35 *Ea.* and 26 *Ta.* spicules using a configuration
 79 similar to that described by Jaya et al^[30–32]. We placed a spicule across a trench that was cut in a steel
 80 plate and ensured that its longitudinal axis was perpendicular to the trench edges (see Figure 4(A)). We
 81 used trenches whose spans were nominally 600 to 800 μm and measured the span of each trench, L , from
 82 optical micrographs (see Table I for a summary and Tables S1 and S2 for measurement details). We then
 83 glued the ends of the spicule to the steel plate so that only the section suspended over the trench remained
 84 exposed.

85 The spicule specimen's undeformed configuration can be described using the orthonormal set of Cartesian
 86 basis vectors $\{\hat{e}_1, \hat{e}_2, \hat{e}_3\}$ (Figure 4(A), (B), and (D)), which correspond to the Cartesian coordinates
 87 $\{x_1, x_2, x_3\}$. The origin of this coordinate system, denoted as \mathcal{O} , is located at the point on the spicule's
 88 central, longitudinal axis directly above the left trench edge (see Figure 4(A)).

89 We cut a notch through part of the spicule's cross-section located mid way across the trench (i.e., at
 90 $x_1 = L/2$) using a focused ion beam (FIB) (see Figure 4(A)–(B) and Section 5.2). A representative
 91 micrograph of a notched spicule is shown in Figure 4(C). Figure 4(D) depicts a schematic representation
 92 of the spicule's cross-section at $x_1 = L/2$ in which the notched region is shown in light blue and the
 93 remaining ligament is shown in dark blue. We refer to the apex or tip of the notch as the notch root. The
 94 notch root is a straight line segment that is parallel to \hat{e}_3 , see Figure 4(D)). After cutting the notch, we
 95 imaged the spicule using the FIB and measured the diameter of the spicule's cross-section at $x_1 = L/2$,

96 D , and the notch length, a , from the micrographs (see Table I for a summary and Tables S1 and S2 for
measurement details).

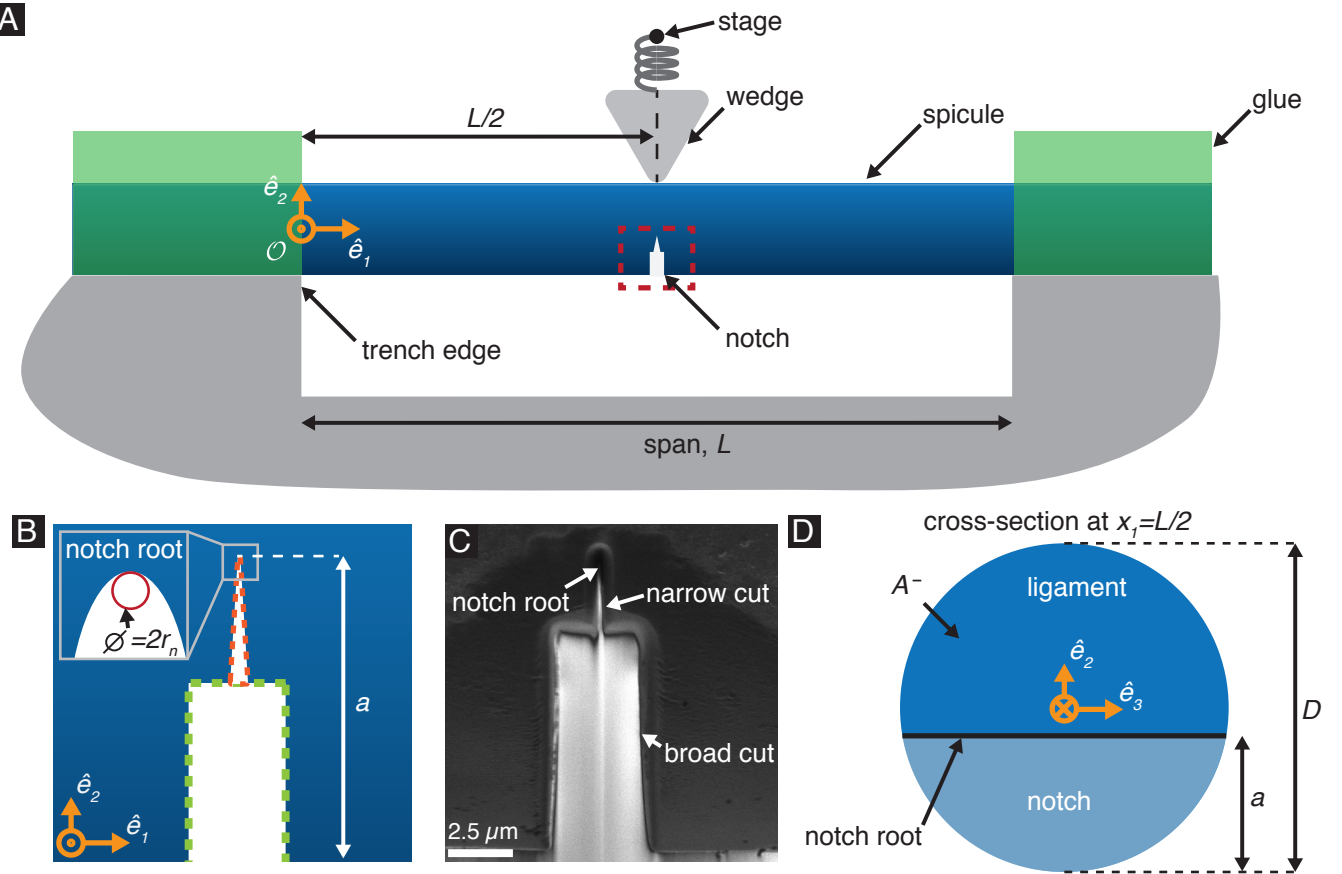


Figure 4. Notched spicule specimen geometry. (A) A schematic of the test configuration. The stage is denoted by a black dot. (B) A magnified view of the region shown in the red rectangle in (A) showing the notch geometry. The broad cut that was made using a high accelerating current is marked in green and the narrow cut that was made using the low accelerating current is marked in orange. (C) A scanning electron micrograph of the notch cut in a representative *Ea*. spicule. (D) A schematic of the spicule's cross-section at $x_1=L/2$ after notching. The notch root is straight and parallel to \hat{e}_3 . The notch length is a . The remaining ligament has a cross sectional area A^- .

97

98 We positioned the spicule underneath a steel wedge so that the apex of the wedge was located at $x_1 = L/2$
99 on the opposite side of the spicule from the notch (see Figure 4(A)). We used a motorized translation
100 stage to push the wedge into the spicule in $1\ \mu\text{m}$ displacement increments at a rate of $1\ \mu\text{m/s}$. The
101 displacement of the translation stage is $-w_s \hat{e}_2$ (see Figure 5(A)). We also measured the displacement
102 of the spicule's cross-section beneath the wedge, w_0 (see Figure 5(A)). The device used to perform the
103 flexural tests is described in detail in^[23,33].

104 The wedge was attached to a cantilever whose stiffness was measured before the test. We measured the
105 deflection of the cantilever using a fiber optic displacement sensor. The force acting on the spicule is

¹⁰⁶ $-F\hat{e}_2$. We computed F using the cantilever's stiffness and the measured deflection^[23]. Since spicule
¹⁰⁷ specimens with longer notches require less force to fracture, we used cantilevers with different stiffnesses
¹⁰⁸ depending on the spicule diameter and notch length. The cantilever stiffnesses in our experiments ranged
¹⁰⁹ from 88 to 9100 Nm⁻¹.

¹¹⁰ Our test configuration can be thought of as a modification of the “single edge crack round bar bend” (SEC-
¹¹¹ RBB) test described by Bush^[34]. In contrast to the standard SEC-RBB test, in our test the specimen's
¹¹² ends are encastered or fixed rather than supported by rollers.

¹¹³ 2.1 Force-displacement responses of notched spicules

¹¹⁴ Representative $F-w_0$ data for an *Ea.* and *Ta.* spicule are shown as dark gray points in Figure 5(C) and
¹¹⁵ (D), respectively. We observed that F first increases with w_0 up to a value of F_c , at which point there is an
¹¹⁶ abrupt drop in force. We interpret this abrupt drop in force to be the point at which a crack starts growing
¹¹⁷ from the notch root. This event is commonly referred to as “pop-in”^[31,35]. We denote the displacement
¹¹⁸ corresponding to F_c as w_c . The point (w_c, F_c) is shown as a red square in Figure 5(C) and (D) and the
¹¹⁹ values of w_c and F_c for each specimen are given in Tables S1 and S2

¹²⁰ As we continued to load the spicule after pop-in, the crack propagated across the spicule's cross-section
¹²¹ until it completely cleaved the spicule into two pieces. Finally, we unloaded the spicule by moving the
¹²² stage away from the spicule (i.e., in the \hat{e}_2 direction) in 1 μm displacement increments at a rate of 1
¹²³ $\mu\text{m s}^{-1}$. The $F-w_0$ data obtained during unloading are shown as light gray points in Figure 5(C) and (D).

¹²⁴ After the spicule was completely unloaded we dissolved the adhesive on its ends and obtained two sepa-
¹²⁵ rate pieces, which we collected for additional imaging (see Section 2.2).

¹²⁶ 2.2 Fractography

¹²⁷ After testing the *Ea.* and *Ta.* spicule specimens, we imaged their fracture surfaces using a scanning
¹²⁸ electron microscope (see Figure 6(A), (B)). In all *Ea.* and *Ta.* specimens, failure appears to occur via a
¹²⁹ single crack that originates at the notch root. The existence of a single dominant crack is a prerequisite

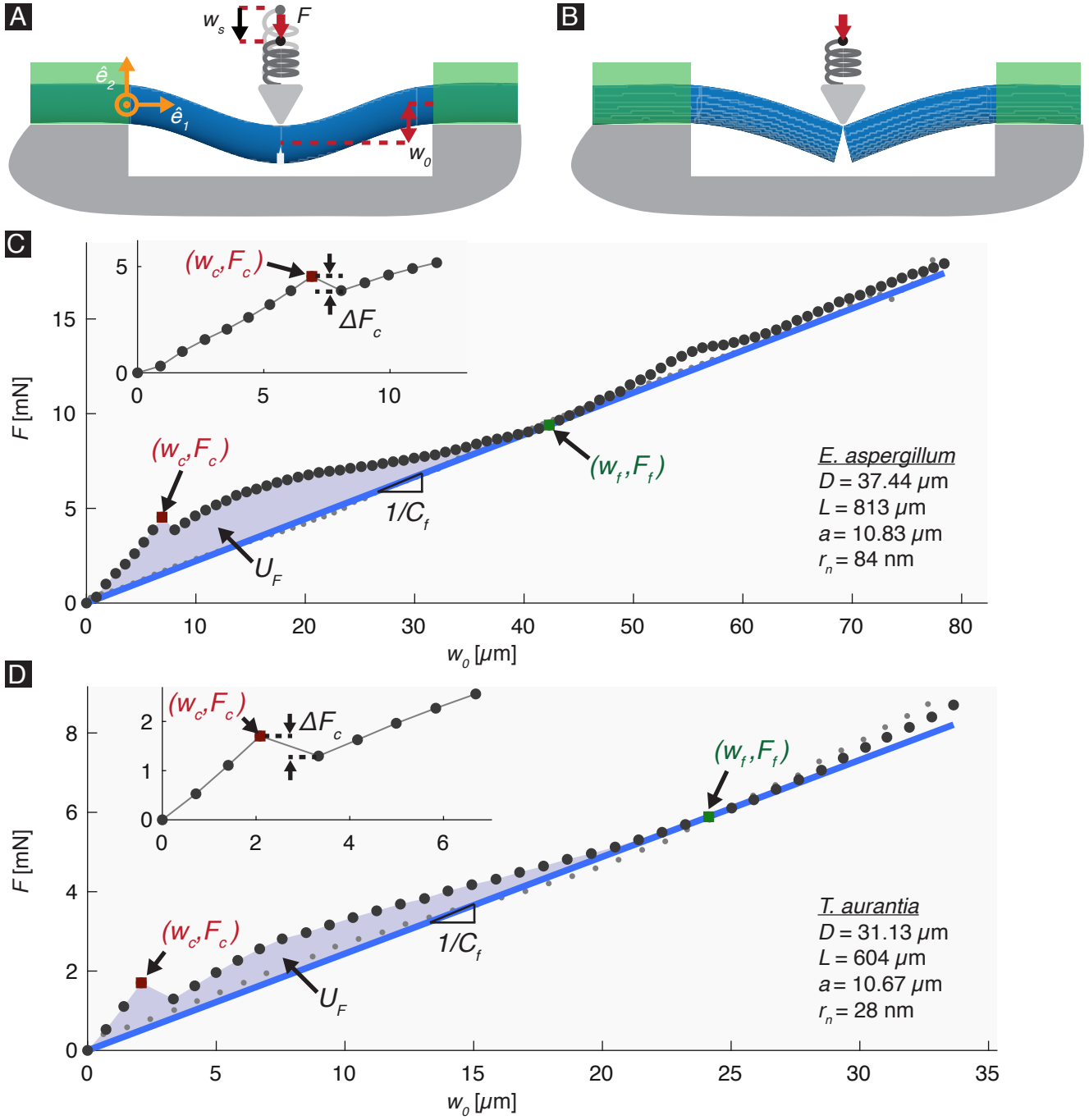


Figure 5. Data obtained from the bending tests. (A) The wedge is used to apply a force $-F\hat{e}_2$. The displacement of the stage is $-w_s\hat{e}_2$ and the corresponding displacement of the spicule's cross-section at $x_1 = L/2$ is $-w_0\hat{e}_2$. The stage is denoted by a black dot. The glue (shown in green) prevents the ends of the spicule from rotating or moving relative to the plate to which it is attached. (B) After the specimen has failed completely, it resembles two cantilevers. (C) The $F-w_0$ response of a representative *Ea*. spicule. (D) The $F-w_0$ response of a representative *Ta*. spicule. The $F-w_0$ data obtained during loading and unloading are shown as dark gray points and light gray points, respectively. Crack initiation (i.e., pop-in) is marked as a red square and has a force and displacement of F_c and w_c . The insets in (C) and (D) show a magnified view of the $F-w_0$ response leading up to pop-in and the drop in force during pop-in, ΔF_c . The point of complete failure is marked with a green square and has a force and displacement of F_f and w_f . The blue line with slope $1/C_f$ is the line that passes through the origin and the point (w_f, F_f) . The shaded region marked U_F in (C) and (D) is the area enclosed between the $F-w_0$ data and this line.

130 to computing the spicules' average crack growth resistance, which we do in Section 2.4.

131 The fracture surfaces of both the *Ea.* and *Ta.* spicules appear to be relatively featureless. In the case of the
132 *Ea.* spicules, this contrasts with the fracture surfaces observed in other SBMs with layered architectures,
133 like nacre and conch shell (see Figure 1 (D), (F)). In these other SBMs the fracture surfaces appear
134 very rough. This roughness is thought to be a signature of the crack arrest and re-nucleation toughening
135 mechanism that occurs when a crack reaches an interface between adjacent layers^[10,36–38]. Specifically,
136 after a crack is arrested at an interface between layers, it often will not continue along the same path
137 as before when it re-nucleates in the next layer. The resulting deflection of the crack path manifests
138 as surface roughness in fractographs. As such, the relatively smooth fracture surface of the *Ea.* spicules
139 suggests that they may not possess the same toughening mechanism(s) associated with these other SBMs.

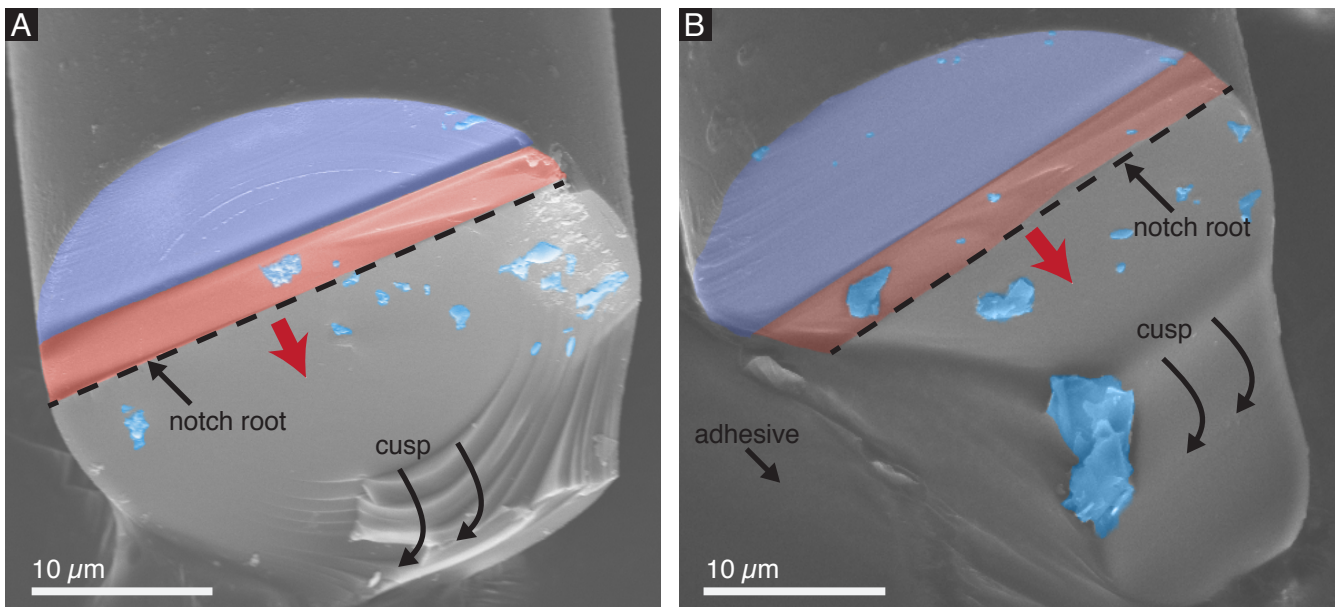


Figure 6. Micrographs of a fractured (A) *Ea.* and (B) *Ta.* spicule. False color is used to mark important features. The purple region in both (A) and (B) corresponds to the coarse (higher current) FIB cut discussed in Section 5.2. The red region in (A) and (B) corresponds to the fine (lower current) FIB cut. The blue regions correspond to debris that we assume collected on the fracture surfaces during specimen preparation. The red arrow denotes the direction of crack growth. The cusp feature in (A) and (B) is a feature of the three-point bending test configuration that appears for both the *Ea.* and *Ta.* spicules. In (B), part of this feature is occluded by the adhesive used to mount the spicule to the aluminum stub.

140

141 The fracture surfaces of both the *Ea.* and *Ta.* spicules have a cusp feature adjacent to where the load is ap-
142 plied (see e.g., Figure 6(A), (B)). This cusp is characteristic of the three point bending configuration^[39]
143 and is a consequence of the compressive stresses caused by the wedge inducing local mixed-mode frac-

¹⁴⁴ ture conditions, which cause the crack to change direction^[40]. The cusp is not a result of a toughening
¹⁴⁵ mechanism caused by the *Ea.* spicules architecture since it also appears in the *Ta.* spicules, which lack
¹⁴⁶ the layered architecture.

¹⁴⁷ 2.3 Measurements of fracture initiation toughness

¹⁴⁸ During pop-in, a crack grows from the notch root in the transverse direction, across the spicule's cross-
¹⁴⁹ section (i.e., in the \hat{e}_2 direction, see Figure 3(B)). We assume that the crack front is straight and parallel
¹⁵⁰ to the notch root (i.e., parallel to \hat{e}_3) and denote the crack length as Δa . The energy release rate G is given
¹⁵¹ by

$$G(\Delta a; w_s) = -\frac{1}{2\sqrt{(a + \Delta a)(D - (a + \Delta a))}} \frac{d\Pi(\Delta a; w_s)}{d\Delta a}, \quad (1)$$

¹⁵² where $\Pi(\Delta a; w_s)$ is the system's potential energy when the crack's length is Δa and the applied displace-
¹⁵³ ment is w_s . For a derivation of Equation (1), see Section S1. It follows from Irwin's analysis of Griffith's
¹⁵⁴ theory of fracture that the necessary condition for crack growth is $G(\Delta a, w_s) \geq R(\Delta a)$, where $R(\Delta a)$ is the
¹⁵⁵ material's crack growth resistance^[40]. We assume that crack growth first occurs when $G(0, w_s) = R(0)$
¹⁵⁶ and w_s is the applied displacement at pop-in. Thus, the fracture initiation toughness $R(0)$ is given by

$$R(0) = -\frac{1}{2\sqrt{a(D-a)}} \left. \frac{d\Pi(\Delta a; w_s)}{d\Delta a} \right|_{\Delta a=0}, \quad (2)$$

¹⁵⁷ where w_s is the applied displacement at pop-in.

¹⁵⁸ For each *Ea.* and *Ta.* spicule that we mechanically tested, we measured $R(0)$ by computing the derivative
¹⁵⁹ in Equation (2) using a computational mechanics model. This model is described in detail in Section
¹⁶⁰ S3. In the computational mechanics model we consider both the *Ea.* and *Ta.* spicules to be made of a
¹⁶¹ homogeneous, linear elastic material. In reality, the *Ea.* spicules contain layers and are therefore not
¹⁶² homogeneous. Therefore, the values of $R(0)$ that we obtain for the *Ea.* spicules should be considered to
¹⁶³ be an *effective* fracture initiation toughness.

¹⁶⁴ The accurate estimation of $R(0)$ using Equation (2) is predicated on the assumption that the notch be-
¹⁶⁵ haves like a sharp crack (i.e., the radius of curvature of the notch root is vanishingly small). It has

been shown that the FIB cutting technique can produce notch root radii that are small enough to act like sharp cracks^[41]. This is supported by additional work^[42] showing that if the notch root radius is less than twice the smallest microstructural length scale, then the measured value of $R(0)$ becomes insensitive to the notch root geometry. The *Ea.* spicules' layers are composed of silica nanoparticles that are approximately 100 nm in diameter^[18]. We take the size of these nanoparticles to be the smallest microstructural length scale present in the *Ea.* spicules. We assume that the *Ta.* spicules have a similar smallest microstructural length scale. This assumption is supported by atomic force microscopy of the *Ta.* spicules^[43]. Therefore, in order for the value of $R(0)$ to be insensitive to the notch root geometry, the radius of curvature of the notch root, r_n , should be less than 200 nm (see Figure 4(B) inset).

We measured r_n for each specimen from scanning electron micrographs by manually selecting three points along the profile of the notch root and fitting a circle to these points (see Tables S1 and S2). The mean value±standard error of r_n for the 35 *Ea.* spicules and 26 *Ta.* spicules was 112±14 nm and 149±15 nm, respectively. We identified 4 *Ea.* spicule specimens and 5 *Ta.* spicule specimens for which r_n exceeded 200 nm, and consequently we did not compute $R(0)$ for these specimens. Additionally, there were 9 *Ea.* spicule specimens for which we were unable to reliably identify the pop-in event by inspecting the F - w_0 response, and therefore could not obtain w_c . Thus, we computed $R(0)$ for 22 *Ea.* spicules and 21 *Ta.* spicules (see Figure 7(A)).

We measured $R(0)$ for the *Ta.* spicules to be 3.76±0.49 Jm⁻² (mean±standard error, $N = 21$) and $R(0)$ for the *Ea.* spicules to be 7.15±1.83 Jm⁻² (mean±standard error, $N = 22$). The measurements of $R(0)$ for each spicule are shown in Figure 7(A) and in Tables S1 and S2. Overall, these values are similar to those expected for glass and other brittle ceramic materials (see Figure 7(A)). In the case of the *Ta.* spicules, the value of $R(0)$ appeared relatively constant regardless of the dimensionless notch length, $\alpha = a/D$. For values of $\alpha > 0.1$, the fracture initiation toughness of the *Ea.* spicules was also relatively constant. However, the *Ea.* spicules displayed a sharp increase in $R(0)$ for $\alpha < 0.1$ (see Figure 7(A)). The largest value of $R(0)$ that we measured was 33.84 Jm⁻² for an *Ea.* spicule specimen with $\alpha=0.07$. The increase in fracture initiation toughness for small values of α suggests that the *Ea.* spicule's architecture is increasing its effective fracture initiation toughness for small flaws or cracks.

We offer the following qualitative explanation for this observed increase in $R(0)$. Recall that the *Ea.*

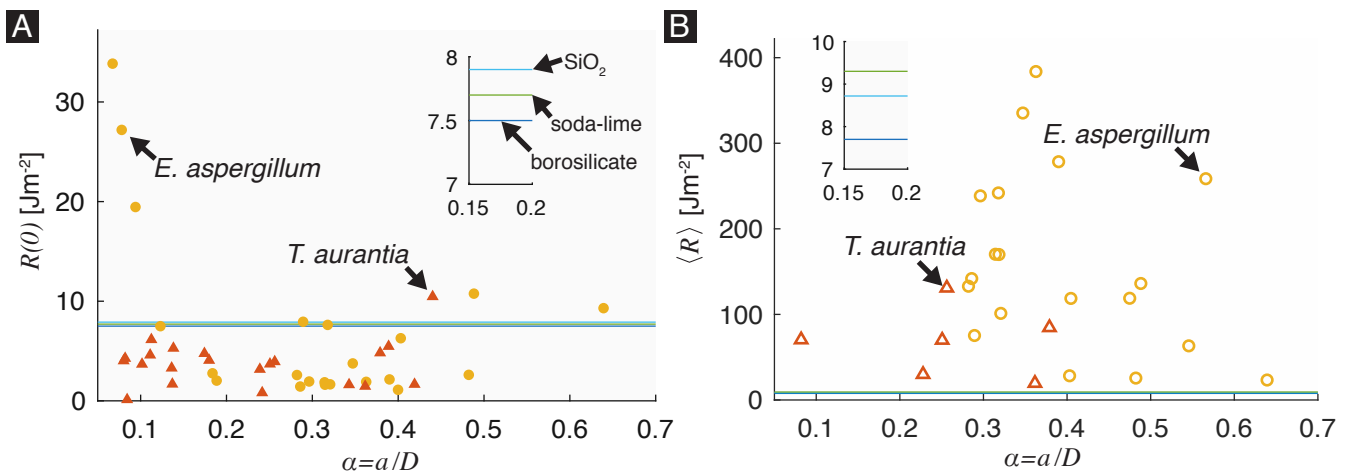


Figure 7. Crack growth resistance of *Ea.* and *Ta.* spicules. (A) Fracture initiation toughness, $R(0)$, of 22 *Ea.* spicules (yellow circles) and 21 *Ta.* spicules (red triangles) versus dimensionless notch length, $\alpha = a/D$. Reference lines are shown corresponding to the fracture initiation toughnesses of three types of synthetic glass measured by^[44]. The inset shows a closer view of these three values. (B) Average crack growth resistance, $\langle R \rangle$, of 19 *Ea.* spicules (hollow yellow circles) and 6 *Ta.* spicules (hollow red triangles) versus α . Reference lines are given that correspond to the average crack growth resistance of the three types of synthetic glass shown in (A). We computed the value of $\langle R \rangle$ from the measurements of the work of fracture provided by^[44]. The inset in (B) shows a closer view of these three values.

spicule's cross-section consists of ≈ 25 cylindrical layers surrounding a large, monolithic core. In a previous work, it was shown that the ratio of the core's diameter to the spicule's diameter is relatively constant with a mean value of 0.41 and a standard deviation of 0.07 ($N=116$)^[11]. From this it can be shown that the value of α at which the notch reaches the core of the spicule is approximately 0.3. Thus, for $\alpha < 0.3$ a crack growing from the notch will initially propagate perpendicular to some of the interlayers. It has been shown that when a crack propagates perpendicular to the spatial variation of material properties in a structure consisting of flat layers of a stiff material that are separated by thin, compliant or weak interlayers, the structure will display enhanced fracture initiation toughness compared to the bulk material^[8, 25, 45]. The toughness enhancement is a result of the energy release rate decreasing when a crack impinges on a compliant or weak interlayer^[8, 45]. This mechanism has been observed experimentally in bioinspired composites^[46, 47] and previous works have speculated that it may also be operating in the *Ea.* spicules^[8, 45]. Our observation that $R(0)$ increases with decreasing α is consistent with the predictions of these models^[8, 25, 45]. For specimens with $\alpha > 0.3$, the notch reaches the silica core of the spicule where there are no interlayers, and the interlayers between the silica layers outside the core are not perpendicular to the initial direction of crack growth. Therefore, in these specimens the spicule would not be able to benefit from the above-mentioned toughness enhancement mechanism. In

210 agreement with this observation, in the *Ea.* spicules with $\alpha > 0.3$, the values of $R(0)$ are similar to those
211 that we measured in the *Ta.* spicules (see Figure 7(A)).

212 2.4 Measurements of average crack growth resistance

213 In our experiment the average crack growth resistance, $\langle R \rangle$ is defined as

$$\langle R \rangle = \frac{1}{D-a} \int_0^{D-a} R(\Delta a) d\Delta a. \quad (3)$$

214 We measured $\langle R \rangle$ using the work of fracture method^[48, 49]. Specifically, it can be shown that

$$\langle R \rangle = 2\gamma_{WOF}, \quad (4)$$

215 where γ_{WOF} is called the work of fracture^[49]. The work of fracture is obtained by fracturing a specimen,
216 measuring the total energy that is consumed by the fracture process, U_F , and dividing that by the total
217 new surface area created^[48]. Because the spicule specimens are cleaved into two pieces by a single crack
218 emanating from the notch root (see Section 2.2), we take the total new surface area created to be twice
219 the cross-sectional area of a specimen's ligament before any crack growth has occurred, A^- (see Figure 4
220 (D)). Therefore, $\langle R \rangle$ is given by

$$\langle R \rangle = U_F / A^-. \quad (5)$$

221 In order to compute $\langle R \rangle$ using Equation (5), the crack must grow in a stable manner throughout the
222 test^[50, 51]. Unstable crack growth events appear as discontinuities in the $F-w_0$ response. The pop-in
223 (marked by a red square in Figure 5(C) and (D)), is an example of such an event. Consequently, $\langle R \rangle$
224 computed using Equation (5) from the $F-w_0$ data will be an overestimate of the actual value of $\langle R \rangle$. Aside
225 from the pop-in event, however, the $F-w_0$ curves shown in Figure 5 are continuous. For that reason, we
226 believe that in our experiments the cracks grow in a predominantly stable manner. Previous studies have
227 attempted to compute the spicule's work of fracture from their $F-w_0$ response^[6, 16]. However, the data
228 presented in these previous studies suggests that the crack growth was not stable and therefore the data

229 in these studies cannot be used to obtain accurate estimates of $\langle R \rangle$.

230 We used the magnitude of the drop in F at pop-in as a criterion for determining which spicule specimens
231 could be used to estimate $\langle R \rangle$. Specifically, we measured the drop in force during pop-in, ΔF_c (see Figure
232 5(C), (D) inset), and compared it to F_c . We considered a test to have predominantly stable crack growth
233 if $\Delta F_c \leq 0.15F_c$. We identified 16 Ea. and 20 Ta. spicules for which $\Delta F_c > 0.15F_c$ and consequently we
234 could not compute $\langle R \rangle$ for these specimens.

235 If the crack grows in a predominantly stable manner then the change in kinetic energy of the spicule
236 during the test is negligible and it can be shown that

$$U_F + U_{ef} = \int_0^{w_f} F dw_0, \quad (6)$$

237 where w_f is the value of w_0 at which the crack has just cleaved the specimen into two pieces and U_{ef}
238 is the elastic energy of the spicule in the completely failed state. The integral on the right hand side
239 of Equation (6) is the work done on the spicule until it has completely failed. In order to evaluate this
240 integral we must identify the (w_0, F) point at which the crack had just cleaved the spicule into two pieces.

241 We assume that if at any point during the test we were to unload the spicule, F would decrease linearly
242 with w_0 until the values of both reached zero. Our rationale for this assumption is that the spicule
243 behaves in a linear elastic fashion when there are no dissipative processes operating (e.g., crack growth).
244 This means that the elastic unloading compliance of the spicule at a point (w_0, F) is given by $C = w_0/F$.
245 Since crack growth invariably increases the elastic unloading compliance of a structure, we know that C
246 should be greatest when the crack has completely cleaved the spicule into two pieces. Thus, we define
247 w_f and the corresponding force, F_f , at which the spicule has just been cleaved into two pieces to be the
248 (w_0, F) point for which C is maximum. The point (w_f, F_f) is shown in Figure 5(C) and (D) as a green
249 square. The line with slope $1/C_f$ that passes through both this point and the origin is also shown in
250 Figure 5(C) and (D) in blue. The values of w_f and F_f for each specimen are given in Tables S1 and S2.

251 In many test configurations, such as the standard single edge crack specimen^[34], $U_{ef} = 0$. However, for
252 the configuration that we use, U_{ef} is nonzero since the specimen's stiffness is finite even after the crack
253 has completely cleaved the specimen into two halves. Specifically, when our specimen has completely

254 failed, the elastic energy is given by $U_{ef} = w_f F_f / 2$. We can therefore simplify Equation (5) and (6) to
 255 get

$$\langle R \rangle = \frac{\int_0^{w_f} F dw_0 - w_f F_f / 2}{A^-}. \quad (7)$$

256 For a specimen with a circular cross-section containing a notch of length a and crack of length Δa , as
 257 shown in Figure 3(B), the area of the intact portion of the specimen's cross-section is

$$A(\Delta a) = \frac{\pi D^2}{4} + \frac{1}{2} (D - 2(a + \Delta a)) \sqrt{(a + \Delta a)(D - (a + \Delta a))} - \frac{D^2}{4} \cos^{-1} \left(1 - \frac{2(a + \Delta a)}{D} \right). \quad (8)$$

258 In Equation (8) we assume that both the notch root and crack front are straight line segments that are
 259 parallel to \hat{e}_3 . We computed $A^- = A(0)$ from Equation (8) using the a and D that we measured from
 260 scanning electron micrographs taken before the flexural tests (see Section 2).

261 For 19 *Ea.* and 6 *Ta.* spicule specimens we computed $\langle R \rangle$ from Equation (7) using trapezoidal integration
 262 of the F - w_0 data up to the point (w_f, F_f) . We found $\langle R \rangle$ to be $160.12 \pm 23.99 \text{ J m}^{-2}$ (mean \pm standard error,
 263 $N=19$) and $67.56 \pm 16.37 \text{ J m}^{-2}$ (mean \pm standard error, $N=6$) for the *Ea.* and *Ta.* spicules, respectively. The
 264 measurements of $\langle R \rangle$ for each spicule are shown in Figure 7(B) and in Tables S1 and S2.

265 2.5 Comparison of toughness enhancements

266 We found that average crack growth resistance of the *Ea.* spicules was higher than that of the *Ta.* spicules.
 267 Specifically, computing the ratio $\langle R \rangle^{(\text{EA})} / \langle R \rangle^{(\text{TA})}$ shows that the architecture increases $\langle R \rangle$ by a factor of
 268 2.37. While this ratio is evidence that the *Ea.* spicule's architecture does enhance toughness, we should
 269 put this enhancement in the context of enhancements observed in other SBMs. We denote the crack
 270 growth resistances of an architected material and its corresponding homogeneous ceramic constituent
 271 with the superscripts (arch) and (hom), respectively. By computing $\langle R \rangle^{(\text{arch})} / \langle R \rangle^{(\text{hom})}$ for nacre, bone,
 272 antler and conch shell using work of fracture data available from literature (see Figure 8(B) and Table 2),
 273 we see that the $\langle R \rangle$ enhancement in the *Ea.* spicules is quite small. For example, $\langle R \rangle^{(\text{arch})} / \langle R \rangle^{(\text{hom})}$ for
 274 the conch shell exceeds 1000; several hundred times larger than the $\langle R \rangle$ enhancement in the *Ea.* spicules.

275 By computing the enhancement in $R(0)$ using the same procedure, we see that $R(0)^{(\text{arch})} / R(0)^{(\text{hom})}$ can

276 be as large as ≈ 200 in these other biological materials (see Figure 8 (A)). In contrast, we measured
277 $R(0)^{(\text{arch})}/R(0)^{(\text{hom})}$ to be only 1.90 for the *Ea.* spicules on average. Even when considering the relatively
278 large increase in $R(0)$ for short notches (see Section 2.3 for details), the maximum enhancement that we
279 observed is on the order of 10. While this increase is similar to those observed in conch and antler it still
280 is quite small compared to nacre—often considered the archetype for tough biological materials. Thus,
281 while the *Ea.* spicules share a common architectural motif with many tough SBMs, our measurements
282 suggest that these seemingly similar architectures do not provide comparable enhancements to either the
283 fracture initiation toughness or average crack growth resistance.

284 Other studies have compared the mechanical behaviors of spicules with layered architecture to synthetic
285 glass fibers^[6, 16, 20, 21, 52], despite the spicules having a lower elastic modulus and a different chemical
286 composition^[20, 53, 54]. Unlike synthetic glass, the *Ea.* spicules are composed of hydrated silica that is
287 precipitated onto a proteinaceous scaffold^[55]. The effect of this scaffold on the mechanical properties
288 of the spicule’s silica is not fully understood. It would therefore not be possible to isolate the effect of
289 the spicule’s layered architecture on its toughness properties by comparing them to synthetic glass fibers.
290 The *Ea.* spicules should instead be compared to a specimen composed of the same biogenic silica but
291 which is monolithic. An ideal choice for this homogeneous control material would be a section of the
292 solid silica core of the *Ea.* spicules. However, so far we have not successfully obtained a large enough
293 section of the *Ea.* spicule core to perform fracture tests. Therefore, we chose the *Ta.* spicules as what we
294 believe to be the next best alternative.

295 3 Discussion

296 Toughness enhancements in SBMs are often caused by multiple mechanisms that are triggered as a crack
297 interacts with the features of the material’s architecture^[15, 27, 61]. For example, in nacre and other mollusk
298 shells one important toughening mechanism is crack arrest^[15, 62, 63]. This phenomenon occurs when a
299 crack impinges on a weak interface between two layers and requires more energy to resume propagation
300 in the adjacent, undamaged layer. Often, the arrest of a crack will be accompanied by crack deflec-
301 tion along the interface between the adjacent layers. Based on the jagged fracture surfaces observed

Table 2. Summary of SBM crack growth resistance data used to compute the toughness metrics in Figure 8. Statistical data, such as standard deviation (s.d.) standard error (s.e.) and sample number (N) are included when available.

Material	$R(0)$ [Jm $^{-2}$]	$\langle R \rangle$ [Jm $^{-2}$] ^{c)}	Ref.
nacre (<i>Pinctada margaritifera</i>)	587 \pm 189 (mean \pm s.d., N =14)	2068 \pm 544 (mean \pm s.d., N =12)	[14]
nacre (<i>Pinctada margaritifera</i>)	—	3300 \pm 78 (mean \pm s.e.) ^{d)}	[15]
nacre (<i>Pinctada margaritifera</i>)	—	2880 \pm 260 (mean \pm s.d.) ^{d)}	[7]
bone (<i>Homo sapiens</i>)	50–200	11250 ^{e)}	[36]
bone (<i>Homo sapiens</i>)	224 \pm 2 (mean \pm s.d., N =7) ^{f)}	—	[28]
bone (<i>Papio anubis</i>)	—	15520 \pm 2900 (mean \pm s.d., N =3)	[37]
bone ^{a)}	—	8000 \pm 524 (mean \pm s.e.) ^{d)}	[15]
antler (<i>Cervus canadensis</i>)	100 ^{e)}	14000 ^{e)}	[29]
conch (<i>Strombus gigas</i>)	25 \pm 7 (mean \pm s.d., N =4)	26000 \pm 14000 (mean \pm s.d., N =8)	[59]
calcite ^{b)}	\approx 3	—	[56]
limestone	—	22	[57]
hydroxyapatite ^{b)}	\approx 10	—	[56]
hydroxyapatite	—	140	[58]

^{a)} The authors of this work did not specify the genus and species from which the bone specimens were obtained;

^{b)} Approximate values are given because the data was taken from a graph showing ranges of property values;

^{c)} Values were obtained for the work of fracture, γ_{WOF} , and were used to compute $\langle R \rangle = 2\gamma_{WOF}$;

^{d)} The number of specimens was not given in the referenced work;

^{e)} Values estimated from R -curve data;

^{f)} The reference provides the mode I stress intensity factor, K_I , at crack growth initiation. From this we estimated $R(0)$ to be K_I^2/E , where E is the Young's modulus^[36]. We take the value of E to be 18.6 GPa as per^[60].

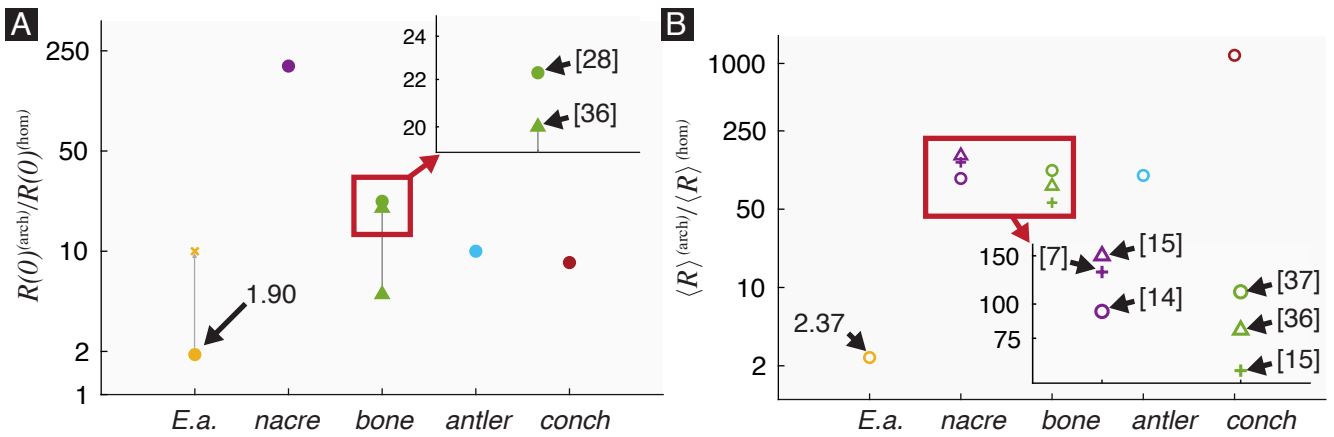


Figure 8. Comparison of the *Ea.* spicule's toughness enhancement to the toughness enhancements of other SBMs with layered architectures. (A) The initiation toughness enhancement metric $R(0)^{(\text{arch})}/R(0)^{(\text{hom})}$ of the *Ea.* spicules and other SBMs with layered architectures. We used the value $R(0)^{(\text{hom})} = 3 \text{ Jm}^{-2}$ of calcite as the control material for nacre and conch^[56], and $R(0)^{(\text{hom})} = 10 \text{ Jm}^{-2}$ of hydroxyapatite^[56] as the control material for bone and antler. For *Ea.*, the solid circle represents the average and the cross represents the approximate value of the maximum enhancement which we observed for very short notches. (B) The average toughness enhancement metric $\langle R \rangle^{(\text{arch})}/\langle R \rangle^{(\text{hom})}$ of the *Ea.* spicules and other SBMs with layered architectures. We used the value $\langle R \rangle^{(\text{hom})} = 11 \text{ Jm}^{-2}$ of limestone as the control material for nacre and conch^[57], and $\langle R \rangle^{(\text{hom})} = 70 \text{ Jm}^{-2}$ of hydroxyapatite^[58] as the control material for bone and antler. In both (A) and (B), the values of $R(0)$ and $\langle R \rangle$ for nacre, bone, antler, and conch (*S. gigas*) were obtained from the literature (see Table 2). The multiple values for bone in (A) and for nacre and bone in (B) correspond to experiments performed by different research groups. The two green triangles connected by a line in (A) correspond to the range of values reported by^[36]. The references from which the data points were obtained are annotated in the insets. Note that in both (A) and (B) the toughness enhancement metrics are plotted using a logarithmic scale.

in previous studies of *Ea.* spicules (see Figure 2(C)), it has been speculated that the spicules *may also* benefit from toughening through crack arrest and re-nucleation^[5, 16]. However, the fracture surfaces of the notched spicules (see Section 2.2) are relatively featureless (see Figure 6(A)). From these results and the relatively small toughness enhancement observed in the *Ea.* spicules it is clear that the *Ea.* spicule's architecture does not trigger the same toughening mechanisms observed in these other SBMs. Or, if the same toughening mechanisms are triggered, they are not as effective in the *Ea.* spicules.

To understand the difference between the toughening mechanisms operating in the *Ea.* spicules and in SBMs like nacre we performed virtual experiments using a regularized variational fracture (RVF) method (see Section S4 for details). These virtual experiments allowed us to predict the mechanical behaviors of and crack paths in materials with layered architectures. Specifically, we used the RVF method to simulate crack growth in a material with flat/planar layers, like those which appear in nacre, and a material with cylindrical layers, like in the *Ea.* spicules.

Our model material with a planar layered architecture consists of a notched beam with a rectangular cross-

315 section whose width $W = 1$ mm, thickness $H = 1$ mm and length $L = 5$ mm. The beam is composed
316 of two layers separated by a thin “interlayer” (see **Figure 9** (A)). Similarly, our model material with a
317 cylindrical layered architecture consists of a notched beam with a cylindrical cross-section composed of
318 two layers separated by a cylindrical interlayer (see **Figure 9** (B)). We constrained the cylindrical beam
319 to have the same volume as the rectangular beam and therefore its diameter $D = 1.12838$ mm and length
320 $L = 5$ mm. The notch length a in both beams is 0.2 mm.

321 In both beams, the interlayer has a thickness $t = 0.1$ mm and is located a distance $b = 0.2$ mm from the
322 notch root. The Young’s modulus $E = 20.8$ GPa and Poissons ratio $\nu = 0.3$ are the same in both the
323 layers and the interlayer. However, the fracture toughness is $G_b = 500 \text{ Jm}^{-2}$ in the layers and $G_I = 0.5$
324 Jm^{-2} in the interlayer. We loaded the beams in three-point bending by applying a displacement w_0 shown
325 in **Figure 9**.

326 In **Figure 9**(C) we show the load-displacement ($F-w_0$) response of the planar layered beam as well as that
327 of a beam with the same geometry but without the interlayer. The monolithic beam exhibits typical brittle
328 behavior with crack initiation occurring at $F \approx 25$ N leading to a large drop in F , which corresponds to
329 abrupt crack growth, followed by a decrease in F until complete failure. The planar layered beam shows
330 an almost identical response until the peak load is reached and first load drop occurs. After the first load
331 drop, however, the load again increases before a second load drop occurs leading to complete failure.
332 The crack path for the planar layered beam at $w_0 = 0.16$ mm is shown in **Figure 9**(D). By examining the
333 crack path at different values of w_0 , we observe three stages of crack growth:

- 334 1. A crack initiates at the peak load and grows until it reaches the interlayer. This corresponds to the
335 first load drop from $F \approx 25$ N to $F \approx 9$ N. Once the crack reaches the interlayer, it is arrested.
- 336 2. The load then increases from $F \approx 9$ N to $F \approx 10$ N. During this increase, some amount of interfacial
337 fracture occurs (see **Figure 9** (D)) but the crack does not grow into the second layer. Thus, the
338 increase in load corresponds to the crack being arrested by the weak interface.
- 339 3. Finally, the crack re-nucleates in the second layer, resulting in the second load drop from $F \approx 10$ N
340 to $F \approx 5$ N. After the second load drop, the crack continues to grow through the second layer until
341 complete failure occurs.

342 We computed $\langle R \rangle^{(\text{arch})} / \langle R \rangle^{(\text{hom})}$ from the force-displacement response of the planar layered beam to be
 343 1.18. This toughness enhancement is caused by the combined effects of two toughening mechanisms:
 344 interfacial fracture, and crack arrest and re-nucleation.

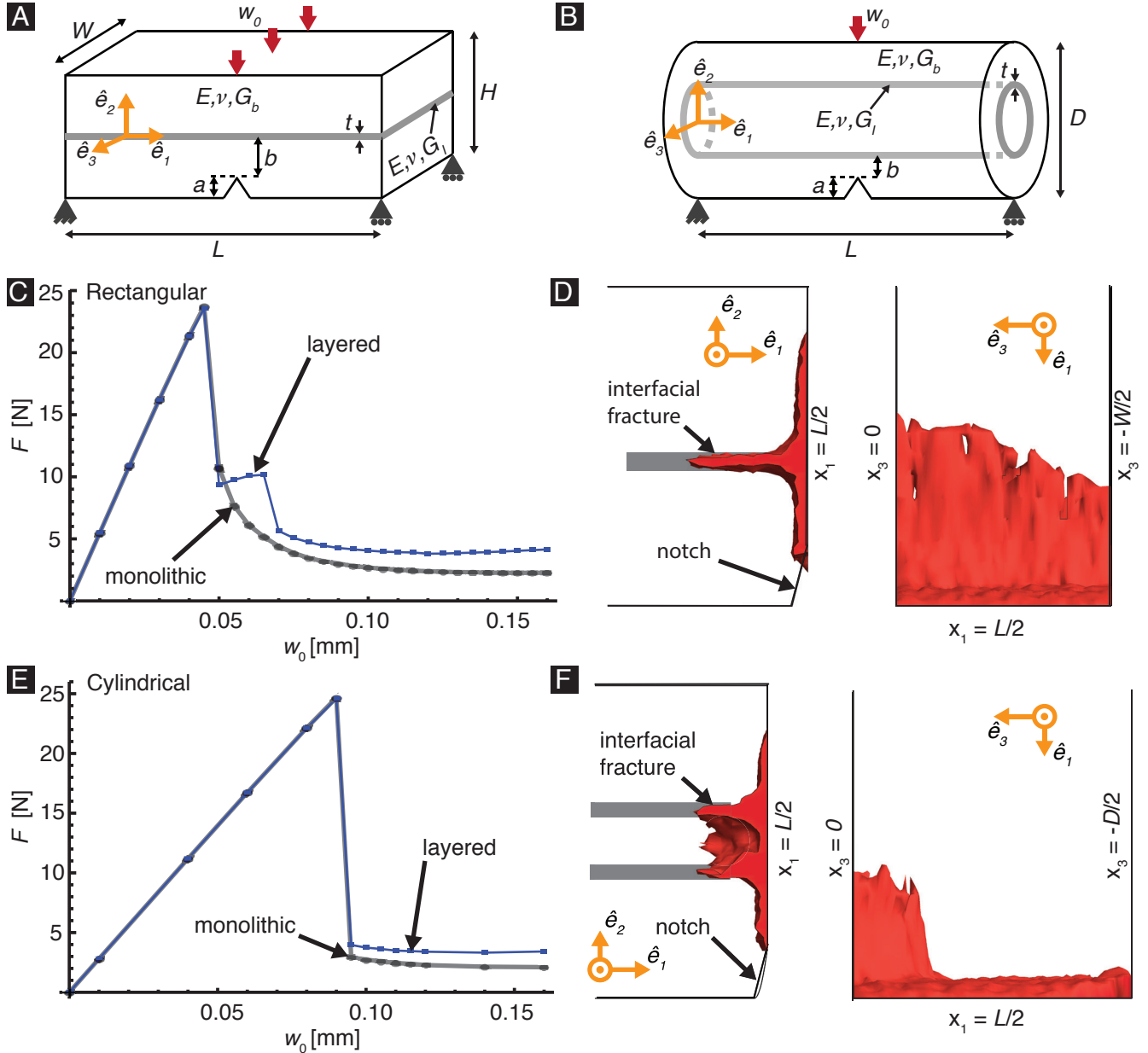


Figure 9. Regularized variational fracture model of beams with planar and cylindrical layered architectures. (A) Geometry of the notched layered beam with one planar interlayer shown in gray. (B) Geometry of the notched cylindrical layered beam with one cylindrical interlayer shown in gray. (C) Load displacement ($F-w_0$) response of the planar layered beam loaded in three-point bending. (D) Crack paths in the planar layered beam as seen from the planes whose normal vectors are \hat{e}_3 and \hat{e}_2 . The red region corresponds to the crack path predicted by the RVF calculations at a displacement $w_0 = 0.16$ mm. (E) $F-w_0$ response of the cylindrical layered beam loaded in three-point bending. (F) Crack paths in the cylindrical layered beam as seen from the planes whose normal vectors are \hat{e}_3 and \hat{e}_2 . The red region corresponds to the crack path predicted by the RVF calculations at a displacement $w_0 = 0.16$ mm. The gray curves in (C) and (E) correspond to monolithic beams with the same geometry and bulk properties.

345 In the case of the cylindrical layered beam, we observed that the F - w_0 response is almost identical to that
346 of its corresponding monolithic beam (see Figure 9(E)). By examining the crack path for the cylindrical
347 layered beam at different values of w_0 (e.g., see Figure 9(F)) we observed that interfacial fracture occurs
348 to roughly the same extent as in the planar layered beam. This results in a small toughness enhancement,
349 $\langle R \rangle^{(\text{arch})} / \langle R \rangle^{(\text{hom})}$, of 1.05. However, unlike the planar layered beam, the crack does not become arrested
350 at the interlayer. The absence of the crack arrest and re-nucleation toughening mechanism explains
351 why the toughness enhancement in the cylindrical layered beam is substantially lower than in the planar
352 layered beam.

353 From this we conclude that while interfacial fracture does enhance the toughness of the cylindrically lay-
354 ered beam, its effect is small compared to the arrest and re-nucleation mechanism that occurs in the planar
355 layered beam. This difference in toughening mechanisms could explain why the toughness enhancement
356 is so much smaller for the *Ea.* spicules than for other SBMs with planar layered architectures.

357 4 Conclusion

358 The surprisingly limited toughness enhancement provided by the *Ea.* spicule's architecture reminds us
359 that it is important to measure each SBM's toughness properties rather than categorizing it as tough solely
360 based on the existence of a layered architecture. Furthermore, the contrast between our findings and
361 previous speculations that the *Ea.* spicule's layers enhance their toughness shows that the understanding
362 of the relationship between layered architectures and toughness enhancement is not yet complete. By
363 showing the extreme variability of the toughness enhancements that are provided by different layered
364 architectures (see Section 2.5 and Figure 8), we hope to galvanize interest in developing a more complete
365 understanding of this relationship. A better understanding of this structure-property relationship is crucial
366 for developing useful bio-inspired designs and avoiding the pitfalls of naive biomimicry.

367 **5 Methods**

368 **5.1 Spicule specimen preparation**

369 *Euplectella aspergillum* skeletons were received dried with the organic tissue removed (see Figure 2(A)).

370 We removed spicules from the basal portion of the skeleton using tweezers and cut \approx 5 mm sections from

371 roughly the midpoint along their length using a razor blade. *Tethya aurantia* spicules were received dried

372 and separated from the sponge's organic tissue. We inspected the *Ea.* and *Ta.* spicules using a polarized

373 light microscope and discarded specimens that were visibly cracked or damaged.

374 All specimens were stored in dry conditions prior to testing. We are aware that the mechanical properties

375 of some SBMs can change substantially if they are soaked in water before testing. For example, the work

376 of fracture of nacre that has been soaked in artificial seawater is 137% higher than that of the same nacre

377 stored in dry conditions^[14]. The soaking procedure is thought to restore the organic phases within them

378 to their native, hydrated state. However, in Supplementary Information S2, we compare the Young's

379 modulus and bending failure strain of *Ea.* spicule specimens stored in wet and dry conditions and find

380 no significant difference between the two (see Supplementary Information S2 for statistical analysis).

381 Motivated by these results, we chose to test the spicules in their as-received, dry state.

382 **5.2 Spicule notching procedure**

383 We cut notches in the spicules using a focused ion beam (FIB) and a procedure similar to that described

384 in^[32]. Before notching, we coated the spicules in 10 nm of carbon to prevent charge accumulation during

385 the cutting procedure. We cut each notch in two steps. First, we used a relatively large accelerating current

386 of 6.5 nA at 30 kV to make a broad cut (marked schematically in green in Figure 4(B)). Then, we used

387 a lower accelerating current of 460 pA at 30 kV to make a narrower cut (marked schematically in orange

388 in Figure 4(B)). The FIB was programmed to make the broad cut between 1.5 and 3 μ m wide depending

389 on the desired depth of the notch. Deeper notches required wider cuts in order to prevent the material

390 that was ablated by the FIB from redepositing on the specimen. The narrow cut was programmed to be

391 250 nm wide. For specimens with very short notches (typically those for which $\alpha < 0.2$), the broad cut

392 was omitted.

393 The actual widths of the cuts differed from these programmed values because the ion beam has a finite
394 width. For each *Ea*. and *Ta*. spicule, we directly measured the widths of both the broad and narrow cuts
395 from scanning electron micrographs (see e.g., Figure 4(C)). Specifically, we measured the width of a
396 cut at the points located closest to and furthest from the notch root. We then averaged the measurements
397 taken at these two points and took this average value to be the width of the cut. Using this procedure we
398 measured the broad cuts to be $3.58 \pm 0.24 \mu\text{m}$ wide (mean \pm standard error, $N = 35$; 24 of which were *Ea*.
399 spicules and 11 of which were *Ta*. spicules) and the narrow cuts to be $501 \pm 21 \text{ nm}$ wide (mean \pm standard
400 error, $N = 61$; 35 of which were *Ea*. spicules and 26 of which were *Ta*. spicules).

401 This two step cutting process and the resulting notch geometry is similar to the procedure for preparing
402 standard edge-notch bending specimens in which a notch is first cut using a diamond saw (broad cut) and
403 then subsequently scored using a razor blade (narrow cut)^[42, 64, 65].

404 Focused ion beams (FIBs) have previously been used to cut notches in micrometer-scale fracture speci-
405 mens^[32, 41, 66, 67]. One concern about this technique is that the cutting mechanism—i.e., material ablation
406 using gallium ions—can cause gallium ion implantation. This implantation alters local composition of
407 the material and therefore could affect the local material properties near the notch root. Furthermore, ion
408 implantation could result in the generation of compressive stresses within the material, which may have
409 an effect on the measured fracture initiation toughness. A previous study^[32] addressed these concerns by
410 measuring the fracture initiation toughness of silicon (100) using FIB notched specimens and comparing
411 these measurements to values obtained by other research groups that used macroscopic specimens and
412 alternative notching procedures^[68]. Their results also match those obtained from fracture tests performed
413 on single crystal silicon specimens that were pre-cracked using a Knoop indenter and loaded in four-point
414 bending^[69]. Thus, they demonstrate that ion implantation does not appear to affect the measurement of
415 fracture initiation toughness.

416 **Acknowledgements** We thank James Weaver for providing us with the *Ta*. spicules and Jarod Ferreira
417 for his help constructing the mechanical testing device. We thank the reviewers of this paper for their
418 insightful comments that led us to connect the observed increase in fracture initiation toughness with
419 decreasing notch length to previous models describing toughness enhancement in materials with layered
420 architectures (Section 2.3). This work was supported by National Science Foundation [Mechanics of

421 Materials and Structures Program, grant number 1562656]; and the American Society of Mechanical
422 Engineers [Haythornthwaite Research Initiation Grant]. M.A.M. received additional support from the
423 NASA Rhode Island Space Grant Consortium.

424 **Author Contributions** M.A.M. and S.K. carried out the experiments. K.V. carried out the computational
425 fracture mechanics simulations. All authors discussed the results and wrote the paper. H.K.
426 designed the research.

427 **Author Information** Correspondence and requests for materials should be addressed to
428 H. K. (haneesh_kesari@brown.edu).

429 **Competing Financial Interests** The authors declare no competing financial interests.

430 References

- 431 [1] Ritchie, R. The conflicts between strength and toughness. *Nature Materials* **10**, 817–822 (2011).
- 432 [2] Wegst, U. G., Bai, H., Saiz, E., Tomsia, A. P. & Ritchie, R. O. Bioinspired structural materials.
433 *Nature Materials* **14**, 23–36 (2015).
- 434 [3] Wang, R., Suo, Z., Evans, A., Yao, N. & Aksay, I. Deformation mechanisms in nacre. *Journal of*
435 *Materials Research* **16**, 2485–2493 (2001).
- 436 [4] Gao, H.-L. *et al.* Mass production of bulk artificial nacre with excellent mechanical properties.
437 *Nature Communications* **8**, 287 (2017).
- 438 [5] Mayer, G. New toughening concepts for ceramic composites from rigid natural materials. *Journal*
439 *of the Mechanical Behavior of Biomedical Materials* **4**, 670–681 (2011).
- 440 [6] Mayer, G. Rigid biological systems as models for synthetic composites. *Science* **310**, 1144–1147
441 (2005).
- 442 [7] Rabiei, R., Bekah, S. & Barthelat, F. Failure mode transition in nacre and bone-like materials. *Acta*
443 *Biomaterialia* **6**, 4081–4089 (2010).
- 444 [8] Kolednik, O., Predan, J., Fischer, F. D. & Fratzl, P. Bioinspired design criteria for damage-resistant
445 materials with periodically varying microstructure. *Advanced Functional Materials* **21**, 3634–3641
446 (2011).
- 447 [9] Munch, E. *et al.* Tough, bio-inspired hybrid materials. *Science* **322**, 1516–1520 (2008).
- 448 [10] Karambelas, G., Santhanam, S. & Wing, Z. N. Strombus gigas inspired biomimetic ceramic com-
449 posites via shell—sequential hierarchical engineered layer lamination. *Ceramics International* **39**,
450 1315–1325 (2013).
- 451 [11] Monn, M. A., Weaver, J. C., Zhang, T., Aizenberg, J. & Kesari, H. New functional insights into the
452 internal architecture of the laminated anchor spicules of euplectella aspergillum. *Proceedings of the*
453 *National Academy of Sciences* **112**, 4976–4981 (2015).

- 454 [12] Rabiei, R., Bekah, S. & Barthelat, F. *Natural Polymers*, 113–149 (Royal Society of Chemistry,
455 London, United Kingdom, 2012).
- 456 [13] Osuna-Mascaró, A. *et al.* The shell organic matrix of the crossed lamellar queen conch shell (*strom-*
457 *bus gigas*). *Comparative Biochemistry and Physiology Part B: Biochemistry and Molecular Biology*
458 **168**, 76–85 (2014).
- 459 [14] Jackson, A., Vincent, J. & Turner, R. The mechanical design of nacre. *Proceedings of the Royal*
460 *society of London Series B: Biological Sciences* **234**, 415–440 (1988).
- 461 [15] Currey, J. Mechanical properties of mother of pearl in tension. *Proceedings of the Royal Society of*
462 *London B: Biological Sciences* **196**, 443–463 (1977).
- 463 [16] Walter, S., Flinn, B. & Mayer, G. Mechanisms of toughening of a natural rigid composite. *Materials*
464 *Science and Engineering: C* **27**, 570–574 (2007).
- 465 [17] Weaver, J. C. *et al.* Hierarchical assembly of the siliceous skeletal lattice of the hexactinellid sponge
466 *euplectella aspergillum*. *Journal of Structural Biology* **158**, 93–106 (2007).
- 467 [18] Aizenberg, J. *et al.* Skeleton of *euplectella* sp.: structural hierarchy from the nanoscale to the
468 macroscale. *Science* **309**, 275–278 (2005).
- 469 [19] Sarikaya, M. *et al.* Biomimetic model of a sponge-spicular optical fiber mechanical properties and
470 structure. *Journal of Materials Research* **16**, 1420–1428 (2001).
- 471 [20] Weaver, J. C. *et al.* Unifying design strategies in demosponge and hexactinellid skeletal systems.
472 *The Journal of Adhesion* **86**, 72–95 (2010).
- 473 [21] Levi, C., Barton, J., Guillemet, C., Le Bras, E. & Lehude, P. A remarkably strong natural glassy
474 rod: the anchoring spicule of the monoraphis sponge. *Journal of Materials Science Letters* **8**,
475 337–339 (1989).
- 476 [22] Wang, X. *et al.* Silica-protein composite layers of the giant basal spicules from monoraphis: basis
477 for their mechanical stability. *Pure and Applied Chemistry* **82**, 175–192 (2010).
- 478 [23] Monn, M. A. & Kesari, H. Enhanced bending failure strain in biological glass fibers due to internal
479 lamellar architecture. *Journal of the Mechanical Behavior of Biomedical Materials* **76**, 69–75
480 (2017).
- 481 [24] Monn, M. A. & Kesari, H. A new structure-property connection in the skeletal elements of the
482 marine sponge *tethya aurantia* that guards against buckling instability. *Scientific Reports* **7**, 1–10
483 (2017).
- 484 [25] Kolednik, O., Predan, J., Fischer, F. & Fratzl, P. Improvements of strength and fracture resistance
485 by spatial material property variations. *Acta Materialia* **68**, 279–294 (2014).
- 486 [26] Bourdin, B., Francfort, G. A. & Marigo, J.-J. Numerical experiments in revisited brittle fracture.
487 *Journal of the Mechanics and Physics of Solids* **48**, 797–826 (2000).
- 488 [27] Barthelat, F. & Espinosa, H. An Experimental Investigation of Deformation and Fracture of Nacre–
489 Mother of Pearl. *Experimental Mechanics* **47**, 311–324 (2007).

- 490 [28] Nalla, R. K., Kruzic, J. J., Kinney, J. H. & Ritchie, R. O. Mechanistic aspects of fracture and r-curve
491 behavior in human cortical bone. *Biomaterials* **26**, 217–231 (2005).
- 492 [29] Launey, M. E., Chen, P.-Y., McKittrick, J. & Ritchie, R. O. Mechanistic aspects of fracture and
493 r-curve behavior in elk antler bone. *Acta Biomaterialia* **6** (2010).
- 494 [30] Jaya B, N., Jayaram, V. & Biswas, S. K. A new method for fracture toughness determination of
495 graded (pt, ni) al bond coats by microbeam bend tests. *Philosophical Magazine* **92**, 3326–3345
496 (2012).
- 497 [31] Jaya, B. N. & Jayaram, V. Crack stability in edge-notched clamped beam specimens: modeling and
498 experiments. *International Journal of Fracture* **188**, 213–228 (2014).
- 499 [32] Jaya, B. N., Kirchlechner, C. & Dehm, G. Can microscale fracture tests provide reliable fracture
500 toughness values? a case study in silicon. *Journal of Materials Research* **30**, 686–698 (2015).
- 501 [33] Monn, M. A., Ferreira, J., Yang, J. & Kesari, H. A millimeter scale flexural testing system for
502 measuring the mechanical properties of marine sponge spicules. *Journal of Visualized Experiments: JoVE* **128**, 1–11 (2017).
- 503 [34] Bush, A. J. Experimentally determined stress-intensity factors for single-edge-crack round bars
504 loaded in bending. *Experimental Mechanics* **16**, 249–257 (1976).
- 505 [35] Paris, P. C. & Sih, G. C. Fracture toughness testing and its applications. *ASTM Committee E-24*
506 **381**, 30–83 (1965).
- 507 [36] Koester, K. J., Ager III, J. & Ritchie, R. The true toughness of human cortical bone measured with
508 realistically short cracks. *Nature Materials* **7**, 672 (2008).
- 509 [37] Liu, D., Wagner, H. & Weiner, S. Bending and fracture of compact circumferential and osteonal
510 lamellar bone of the baboon tibia. *Journal of Materials Science: Materials in Medicine* **11**, 49–60
511 (2000).
- 512 [38] Barthelat, F., Rim, J. E. & Espinosa, H. D. *Applied Scanning Probe Methods XIII*, 17–44 (Springer,
513 New York, New York, USA, 2009).
- 514 [39] Quinn, G. D. *Fractography of Ceramics and Glasses* (National Institute of Standards and Technology, Washington DC, USA, 2007).
- 515 [40] Anderson, T. L. *Fracture Mechanics: Fundamentals and Applications*, 1–96 (CRC press, Boca
516 Raton, Florida, USA, 2017).
- 517 [41] Fett, T., Creek, D., Wagner, S., Rizzi, G. & Volkert, C. A. Fracture toughness test with a sharp notch
518 introduced by focussed ion beam. *International Journal of Fracture* **153**, 85–92 (2008).
- 519 [42] Kübler, J. Fracture toughness of ceramics using the sevnb method: preliminary results. *Proceedings
520 of the 21st Annual Conference on Composites, Advanced Ceramics, Materials, and Structures-B:
521 Ceramic Engineering and Science Proceedings* **18**, 155–162 (1997).
- 522 [43] Weaver, J. C. *et al.* Nanostructural features of demosponge biosilica. *Journal of Structural Biology*
523 **144**, 271–281 (2003).

- 526 [44] Wiederhorn, S. M. Fracture surface energy of glass. *Journal of the American Ceramic Society* **52**,
527 99–105 (1969).
- 528 [45] Fratzl, P., Gupta, H. S., Fischer, F. D. & Kolednik, O. Hindered crack propagation in materials with
529 periodically varying young's modulus—lessons from biological materials. *Advanced Materials* **19**,
530 2657–2661 (2007).
- 531 [46] Zechner, J. & Kolednik, O. Fracture resistance of aluminum multilayer composites. *Engineering
532 Fracture Mechanics* **110**, 489–500 (2013).
- 533 [47] Sistaninia, M., Kasberger, R. & Kolednik, O. To the design of highly fracture-resistant composites
534 by the application of the yield stress inhomogeneity effect. *Composite Structures* **185**, 113–122
535 (2018).
- 536 [48] Nakayama, J., Abe, H. & Bradt, R. Crack stability in the work-of-fracture test: Refractory applica-
537 tions. *Journal of the American Ceramic Society* **64**, 671–675 (1981).
- 538 [49] Sakai, M. & Ichikawa, H. Work-of-fracture of brittle materials with microcracking and crack bridg-
539 ing. *International Journal of Fracture* **55**, 65–79 (1992).
- 540 [50] Tattersall, H. G. & Tappin, G. The work of fracture and its measurement in metals, ceramics and
541 other materials. *Journal of Materials Science* **1**, 296–301 (1966).
- 542 [51] Davidge, R. & Tappin, G. The effective surface energy of brittle materials. *Journal of Materials
543 Science* **3**, 165–173 (1968).
- 544 [52] Johnson, M., Walter, S., Flinn, B. & Mayer, G. Influence of moisture on the mechanical behavior
545 of a natural composite. *Acta Biomaterialia* **6**, 2181–2188 (2010).
- 546 [53] Arasuna, A. *et al.* Structural characterization of the body frame and spicules of a glass sponge.
547 *Minerals* **8**, 88 (2018).
- 548 [54] Woesz, A. *et al.* Micromechanical properties of biological silica in skeletons of deep-sea sponges.
549 *Journal of Materials Research* **21**, 2068–2078 (2006).
- 550 [55] Ehrlich, H. Chitin and collagen as universal and alternative templates in biomineralization. *Inter-
551 national Geology Review* **52**, 661–699 (2010).
- 552 [56] Wegst, U. & Ashby, M. The mechanical efficiency of natural materials. *Philosophical Magazine*
553 **84**, 2167–2186 (2004).
- 554 [57] Carmichael, R. S. *CRC Handbook of Physical Properties of Rocks* (CRC Press, Boca Raton, Florida,
555 USA, 1982).
- 556 [58] Tenhuisen, K. S., Martin, R. I., Klimkiewicz, M. & Brown, P. W. Formation and properties of
557 a synthetic bone composite: hydroxyapatite–collagen. *Journal of Biomedical Materials Research
558 Part A* **29**, 803–810 (1995).
- 559 [59] Kuhn-Spearing, L. *et al.* Fracture mechanisms of the strombus gigas conch shell: implications for
560 the design of brittle laminates. *Journal of Materials Science* **31**, 6583–6594 (1996).

- 561 [60] Rho, J. Y., Ashman, R. B. & Turner, C. H. Young's modulus of trabecular and cortical bone material:
562 ultrasonic and microtensile measurements. *Journal of biomechanics* **26**, 111–119 (1993).
- 563 [61] Launey, M. E. & Ritchie, R. O. On the fracture toughness of advanced materials. *Advanced Mate-*
564 *rials* **21**, 2103–2110 (2009).
- 565 [62] Jackson, A., Vincent, J. & Turner, R. The mechanical design of nacre. *Proceedings of the Royal*
566 *society of London. Series B. Biological sciences* **234**, 415–440 (1988).
- 567 [63] Kamat, S., Su, X., Ballarini, R. & Heuer, A. Structural basis for the fracture toughness of the shell
568 of the conch *strombus gigas*. *Nature* **405**, 1036–1040 (2000).
- 569 [64] Rocha, C. V. & Da Costa, C. A. Effect of notch-root radius on the fracture toughness of composite
570 *si 3 n 4* ceramics. *Journal of Materials Engineering and Performance* **15**, 591–595 (2006).
- 571 [65] Damani, R., Gstrein, R. & Danzer, R. Critical notch-root radius effect in senb-s fracture toughness
572 testing. *Journal of the European Ceramic Society* **16**, 695–702 (1996).
- 573 [66] Ochiai, S., Kuboshima, S., Okuda, H., Morishita, K. & Tsushima, E. Fracture behavior and fracture
574 toughness of pitch-based carbon fiber with an artificial notch introduced by a focused ion beam.
575 *Composite Interfaces* **21**, 265–279 (2014).
- 576 [67] Morishita, K. *et al.* Fracture toughness of a crystalline silicon carbide fiber (tyranno-sa3®). *Journal*
577 *of the American Ceramic Society* **89**, 2571–2576 (2006).
- 578 [68] Ritchie, R. O. Failure of silicon: Crack formation and propagation. In *13th Workshop on Crystalline*
579 *solar cell materials and processes*, vol. 42 (2003).
- 580 [69] Chen, C. P. & Leipold, M. H. Fracture toughness of silicon. *American Ceramic Society Bulletin* **59**,
581 469–472 (1980).